Predictive approach of the size effect of PFRC simulated by using a softening function

J.C. Gálvez
Departamento de Ingeniería Civil: Construcción, E.T.S de Ingenieros de Caminos, Canales y Puertos
Universidad Politécnica de Madrid, Madrid, Spain.

F. Suárez
Departamento de Ingeniería Mecánica y Minera
Universidad de Jaén, Jaén, Spain.

A. Enfedaque & M.G. Alberti
Departamento de Ingeniería Civil: Construcción, E.T.S de Ingenieros de Caminos, Canales y Puertos
Universidad Politécnica de Madrid, Madrid, Spain.

ABSTRACT: The size effect on plain concrete specimens is well known and can be correctly captured when performing numerical simulations by using a well characterised softening function. Nevertheless, in the case of polyolefin-fibre-reinforced concrete (PFRC), this is not directly applicable, since using only diagram cannot capture the material behaviour on elements with different sizes due to dependence of the orientation factor of the fibres with the size of the specimen. In previous works, the use of a trilinear softening diagram proved to be very convenient for reproducing fracture of polyolefin-fibre-reinforced concrete elements, but only if it is previously adapted for each specimen size. In this work, a predictive methodology is used to reproduce fracture of polyolefin-fibre-reinforced concrete specimens of different sizes under three-point bending. Fracture is reproduced by means of a well-known embedded cohesive model, with a trilinear softening function that is defined specifically for each specimen size. The fundamental points of these softening functions are defined a priori by using empirical expressions proposed in past works, based on an extensive experimental background. Therefore, the numerical results are obtained in a predictive manner and then compared with a previous experimental campaign in which PFRC notched specimens of different sizes were tested with a three-point bending test setup, showing that this approach properly captures the size effect, although some values of the fundamental points in the trilinear diagram could be defined more accurately.

1 INTRODUCTION

Size effect on plain concrete is well known and is the reason why fracture develops at lower values of the nominal strength when the size of a concrete specimen increases while keeping the same proportions (Bažant 1984). The size effect in fracture of plain concrete is numerically reproduced by means of a cohesive zone formulation that uses a well-characterised softening diagram (Bažant & Planas 1997, Planas, Guinea, & Elices 1999, Jirásek, Rolshoven, & Grassl 2004). The cohesive crack model proposed by Hillerborg can be considered as the most realistic among simple models when quasi-brittle fractures are studied (Bažant & Yu 2009).

Steel fibres as reinforcement in concrete has been used and studied for decades (Ward & Li 1991, Di Prisco, Lamperti, Lapolla, & Khurana 2008), being boosted in recent years, and the range of fibres used for this purpose has increased (Shah & Rangan 1971, Zollo 1997, Banthia & Gupta 2006, Brandt 2008), with polyolefin fibres being one of the most recent types. The use of polyolefin-fibre-reinforced concrete (PFRC) is growing in recent years, due to its good mechanical behaviour and the fact that it reduces and, in some cases, even eliminates some of the problems observed in steel-fibre-reinforced concrete (SFRC) such as corrosion, sensitivity to magnetic fields, or wear and tear of machinery related to its production (concrete pumps and mixers, for example), making PFRC particularly suitable for some uses. The effect of these fibres on the properties of PFRC has been studied in depth during the last years for traditional vibrated concrete (Alberti, Enfedaque, & Gálvez 2015), self-compacting concrete (Alberti, Enfedaque, Gálvez, & Cortez 2020), and in combination with steel fibres (Alberti, Enfedaque, & Gálvez 2017). Many aspects of PFRC are already studied, such as the fibre distribution depending on the production process (Alberti, Enfedaque, Gálvez, & Agrawal 2016) or how it affects fracture in mode I (Alberti, Enfedaque, Gálvez, & Reyes 2017) and mode II (Picazo, Gálvez, Alberti, & Enfedaque 2018). Although this material is starting to count with initial examples of use as a structural material (Alberti, Gálvez, Enfedaque, Carmona, Valverde, & Pardo 2018, Enfedaque, Alberti, Gálvez, Rivera, & Simón-Talero 2018), there is scarce experience with it and the uncertainty on its behaviour in real engineering works under certain situations. One of the key aspects that must be clarified is the size effect; especially to fill the gap if the material properties measured at a laboratory scale are to be used for designing larger structures.

There is not much information about the size effect in fibre-reinforced concrete (FRC), especially in the case of PFRC. In the case of SFRC, some studies can be found (di Prisco, Felicetti, Lamperti, & Menotti 2004, Yoo, Banthia, Yang, & Yoon 2016), and in the case of PFRC, an experimental campaign has been recently carried out (Picazo, Alberti, Gálvez, Enfedaque, & Vega 2019), which has shown that the nominal strength at the limit of proportionality is governed by the matrix (concrete), and the post-cracking residual strength is governed by the fibres.

In previous works, the use of a cohesive zone formulation fed with a trilinear softening curve has proven to be very convenient for reproducing the fracture process in FRC (Enfedaque, Alberti, Gálvez, & Domingo 2017), but it must be adapted depending on several factors such as the fibre length, the fibre proportion (Alberti, Enfedaque, Gálvez, & Reyes 2017), and the specimen size (Suárez, Gálvez, Enfedaque, & Alberti 2019). The adopted trilinear softening diagram describes the contribution of matrix and fibres in the fracture process which, due to the different elastic moduli of both materials, begin to significantly work at different stages of load transmission. Considering the trilinear diagram shown in Figure 1, the initial point t identifies the fracture of the concrete matrix, k the point at which the contribution of fibres starts to predominate over the contribution of the matrix, r the maximum remanent contribution of fibres, and f the eventual failure of the material.

In (Alberti, Enfedaque, Gálvez, & Reyes 2017), some parameters of the PFRC mix were identified, and some expressions were also proposed to define the fundamental points of the trilinear diagram (k and r points). In (Enfedaque, Alberti, & Gálvez 2019) the length and orientation of fibres were observed as key parameters to define the trilinear diagram, also identifying a higher threshold of the PFRC behaviour obtained testing specimens with long fibres oriented in the optimum direction.

There are some approaches and models to simulate fracture. In many cases, these models are calibrated using the experimental results of the test simulated, but this does not guarantee that the parameters represent any other case different from the one under study. From this point of view, the most interesting approach consists of finding models that can reproduce fracture in a predictive way, that is, a model that is fed with parameters obtained by experimental tests that are different from the loading case that wants to be simulated. This type of model is considered more representative of the material than a specific loading case.

The main aim of this contribution is to reproduce fractures on different size specimens of PFRC using a predictive approach. A cohesive model and a softening diagram that corresponds to a trilinear function defined a priori was employed. Using the knowledge obtained in previous works, the coordinates of each of the fundamental points t, k, r and f were identified. To do this, the experimental results of (Picazo, Alberti, Gálvez, Enfedaque, & Vega 2019) were reproduced and compared through a finite element analysis by using an embedded cohesive crack formulation. In the following sections, the experimental work used as a reference of the size effect in PFRC is briefly described, then the main features of the embedded cohesive crack model used to numerically reproduce fracture are presented, and the trilinear softening functions used with each specimen size are obtained by means of the expressions proposed in (Alberti, Enfedaque, Gálvez, & Reyes 2017). Therefore, in the final part of this paper some conclusions are highlighted.

2 EXPERIMENTAL BENCHMARK

The campaign described in (Picazo, Alberti, Gálvez, Enfedaque, & Vega 2019) was used to compare with the nuemrical simulations. For a detailed description of this campaign, the reader is addressed to the referenced work. Table 1 shows the concrete composition, which corresponds to a self-compacting concrete with 10 kg of fibres per m^3 (SCC10).

Concrete reinforcement consists of 48 mm long polyolefin macrofibres with an embossed surface. The main properties of these fibres can be consulted in Table 2. More information on these fibres can be found in (Alberti, Enfedaque, & Gálvez 2015).

The experimental campaign of reference involved three-point bending tests carried out on three samples of each size, following the guidelines of

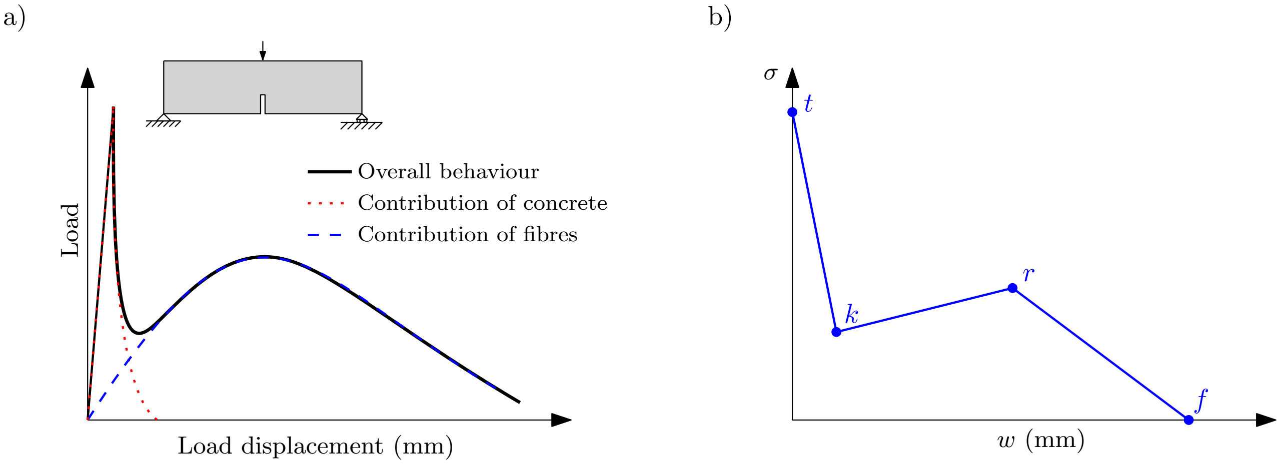

Figure 1: (**a**) Load–displacement diagram obtained in a three-point bending test with a PFRC specimen; (**b**) trilinear softening diagram.

Table 1: Concrete composition.

Material	SCC10
Cement (kg/m^3)	375
Limestone (kg/m^3)	200
Water (kg/m^3)	188
w/c	0.5
Gravel (kg/m^3)	245
Grit (kg/m^3)	367
Sand (kg/m^3)	918
Superplasticiser (% cement weight)	1.25
PF48 (kg/m^3)	10

Table 2: Fibres properties.

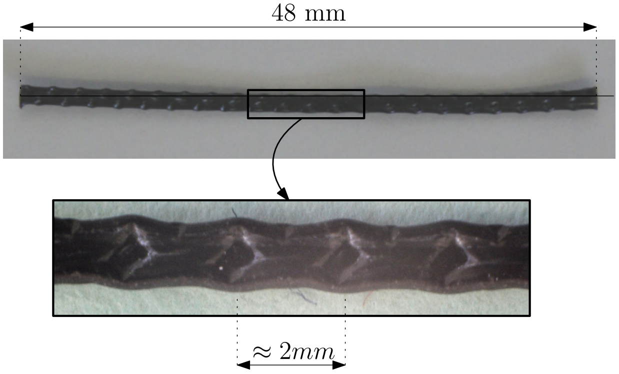

Material density (g/cm^3)	0.910
Eq. diameter (mm)	0.903
Tensile strength (MPa)	>500
Modulus of elasticity (GPa)	>9

the EN-14651 standard (European Committee for Standardization 2007) (except for the specimen sizes and notch dimensions). Figure 2 shows a schematic drawing of the experimental setup, and Table 3 shows the dimensions of the specimens. In all cases, the concrete composition was the same, and 48 mm long polyolefin fibres were used in a proportion of 10 kg/m^3.

The load and the displacement were recorded by the testing machine, and the evolution of the crack mouth opening displacement (CMOD) was measured by means of a digital image correlation system (DIC). To compare the experimental results, two main diagrams were employed: load versus displacement of the application point of the load and load versus CMOD. Figure 2 shows these values in the scheme of a damaged specimen during the test.

Table 3: Specimens' dimensions.

	Length (mm)	Width (mm)	Height (mm)	Notch (mm)
Large	1350	50	300	150
Medium	675	50	150	75
Small	340	50	75	37.5

3 EMBEDDED COHESIVE CRACK MODEL

The crack process is modelled by using the finite element analysis and adapting a formulation based on the cohesive zone approach developed by Hillerborg (Hillerborg, Modéer, & Petersson 1976), inspired by the work of Dugdale (Dugdale 1960) and Barenblatt (Barenblatt 1962). This formulation simulates fracture inside an element using the strong discontinuity approach and was initially developed for concrete (Sancho, Planas, Cendón, Reyes, & Gálvez 2007, Gálvez, Planas, Sancho, Reyes, Cendón, & Casati 2013) but later adapted to brickwork masonry elements (Reyes, Gálvez, Casati, Cendón, Sancho,

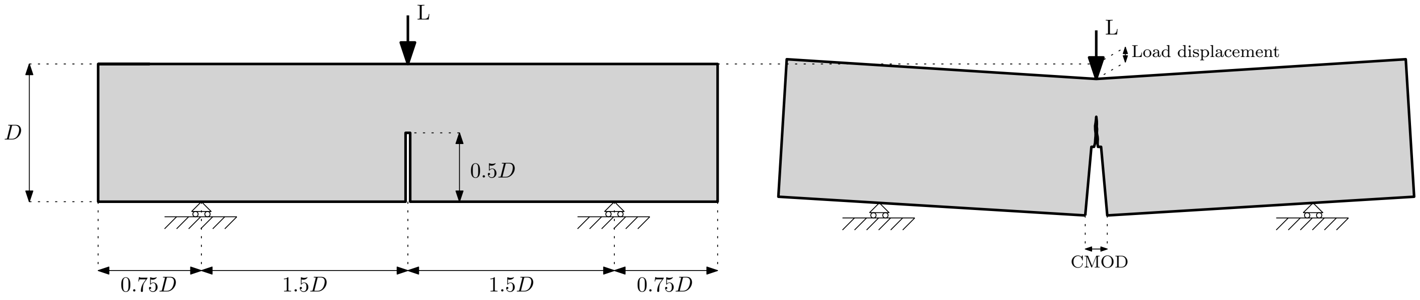

Figure 2: **Left**: scheme of a three-point bending test and specimen geometry; **right**: scheme of crack propagation from the notch tip during the test.

& Planas 2009) and fibre-reinforced cementitious materials (Enfedaque, Alberti, Gálvez, & Domingo 2017, Alberti, Enfedaque, Gálvez, & Reyes 2017, Suárez, Gálvez, Enfedaque, & Alberti 2019).

The cohesive zone approach relies on the experimental evidence that fracture usually develops under a predominant local mode I. Thus, this approach assumes that the cohesive stress vector $\boldsymbol{t}$ is perpendicular to the crack opening and parallel to the crack displacement vector $\boldsymbol{w}$, which is expressed by (1).

$$\boldsymbol{t} = \frac{f(\tilde{w})}{\tilde{w}}\boldsymbol{w} \qquad \text{with } \tilde{w} = \max(|\boldsymbol{w}|) \tag{1}$$

where $f(|\tilde{w}|)$ stands for the material softening function, defined in terms of an equivalent crack opening $\tilde{w}$. This equivalent crack opening stores the maximum historical crack opening to account for possible unloading scenarios. In this case, the softening diagram is defined as trilinear, as shown in Figure 3, and the load–unload branches follow lines towards the origin in all cases. The trilinear diagram is defined by the following expression:

$$\sigma = \begin{cases} f_{ct} + \left(\dfrac{\sigma_k - f_{ct}}{w_k}\right) \cdot w & \text{if } 0 < w \leq w_k \\ \sigma_k + \left(\dfrac{\sigma_r - \sigma_k}{w_r - w_k}\right) \cdot (w - w_k) & \text{if } w_k < w \leq w_r \\ \sigma_r + \left(\dfrac{-\sigma_r}{w_f - w_r}\right) \cdot (w - w_r) & \text{if } w_r < w \leq w_f \\ 0 & \text{if } w > w_f \end{cases} \tag{2}$$

In the finite element models presented later, the embedded cohesive crack formulation is used with constant strain triangular elements. Cracking can only develop in three directions, each parallel to the element sides and at mid height, which guarantees that local and global equilibria are satisfied. Figure 4 shows the only three possible crack paths in an element.

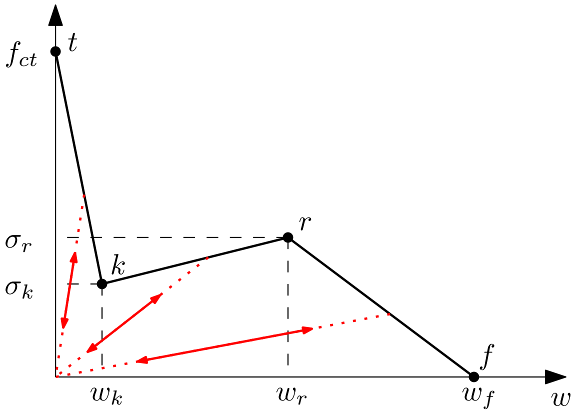

Figure 3: Scheme of a trilinear softening function. Load–unload branches follow a line towards the origin.

Once the crack direction is defined, the element is divided into two parts, A$^+$ and A$^-$, and the stress vector $\boldsymbol{t}$ is constant along the crack, expressed by (3).

$$\boldsymbol{t} = \frac{A}{hL}\boldsymbol{\sigma} \cdot \boldsymbol{n} \tag{3}$$

where A stands for the area of the element, h for the height of the triangle over the side opposite to the solitary node, L for the crack length in the element, and $\boldsymbol{n}$ for the unit vector normal to that side and to the crack. Since the crack is parallel to one side of the triangular element and is placed at mid height, Expression (3) turns into $\boldsymbol{t} = \boldsymbol{\sigma} \cdot \boldsymbol{n}$ (the reader can find more details of this and other aspects of the model in (Sancho, Planas, Cendón, Reyes, & Gálvez 2007)).

The material outside the crack is assumed to be elastic, and the crack displacement vector $\boldsymbol{w}$ is solved considering that the stress tensor can be obtained by subtracting an inelastic part, which considers the contribution of the crack displacement to the elastic prediction computed using the apparent strain by means of (4).

$$\boldsymbol{\sigma} = \boldsymbol{E} : \left[\epsilon^a - \left(\boldsymbol{b}^+ \otimes \boldsymbol{w}\right)^S\right] \cdot \boldsymbol{n} \tag{4}$$

where $\boldsymbol{E}$ is the elastic tangent tensor, ϵ^a the apparent strain vector obtained with the nodal displacements, $\boldsymbol{b}^+$ the gradient vector of the shape function that corresponds to the solitary node, which can be easily obtained in this case by (5), superscript S indicates the symmetric part of the resulting tensor, : the double-dot product ($(\boldsymbol{A} : \boldsymbol{b})_{ij} = A_{ijkl}b_{kl}$), and $\otimes$ the

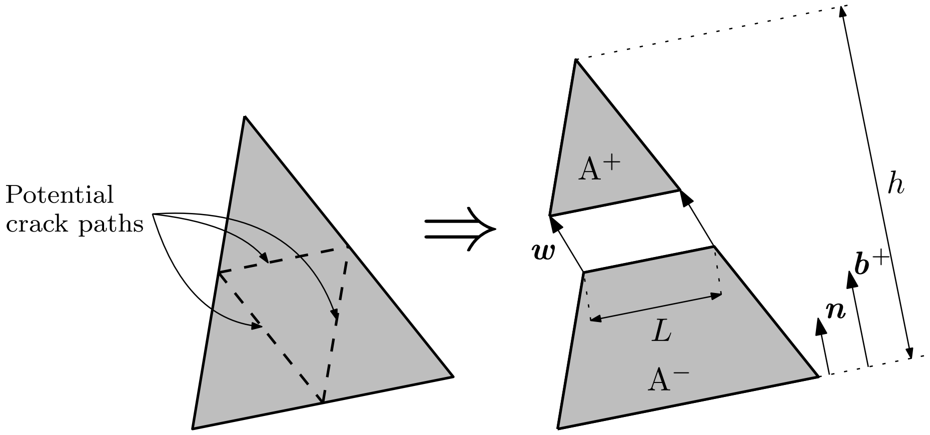

Figure 4: Potential crack paths (**left**) and geometrical definitions of $\boldsymbol{w}$, $\boldsymbol{n}$, and $\boldsymbol{b}^+$ (**right**).

direct product ($(\boldsymbol{a} \otimes \boldsymbol{b})_{ij} = a_i b_j$).

$$\boldsymbol{b}^+ = \frac{1}{h}\boldsymbol{n} \tag{5}$$

Since the stress vector $\boldsymbol{t}$ can be obtained as $\boldsymbol{t} = \boldsymbol{\sigma} \cdot \boldsymbol{n}$, using the expression of $\boldsymbol{\sigma}$ obtained with (4) and the expression of $\boldsymbol{t}$ in terms of the crack opening (1), the following expression is defined:

$$\frac{f(\tilde{w})}{\tilde{w}}\boldsymbol{w} = [\boldsymbol{E} : \boldsymbol{\epsilon}^a] \cdot \boldsymbol{n} - \left[\boldsymbol{E} : \left(\boldsymbol{b}^+ \otimes \boldsymbol{w}\right)^S\right] \cdot \boldsymbol{n}$$

which can be rewritten as

$$\left[\frac{f(\tilde{w})}{\tilde{w}}\mathbf{1} + \boldsymbol{n} \cdot \boldsymbol{E} \cdot \boldsymbol{b}^+\right] \cdot \boldsymbol{w} = [\boldsymbol{E} : \boldsymbol{\epsilon}^a] \cdot \boldsymbol{n} \tag{6}$$

where $\mathbf{1}$ stands for the second-order identity tensor. Using an iterative process (such as the Newton–Raphson method), the crack displacement w that satisfies (6) can be obtained.

This model is implemented using a UMAT subroutine in ABAQUS and, since vectors $\boldsymbol{n}$, $\boldsymbol{b}^+$, crack length L, and the element area A are computed using the nodal coordinates for each element, it reads an external file with this information.

4 DEFINITION OF THE TRILINEAR SOFTENING DIAGRAMS

According to (Alberti, Enfedaque, Gálvez, & Reyes 2017), there are several parameters that can be experimentally measured and help to define the trilinear diagram for the PFRC. Apart from the fracture parameters of plain concrete (G_F and f_t), which define the first part of the diagram, these parameters are the volume of fibres (V_f), the orientation factor (θ) and the percentage of pulled out fibres at the fracture surface ($\%Pulled - out$). With the help of V_f, the angle ϕ can be obtained by means of (7).

$$\phi = -3.6046 + 5.0625 \cdot \left(1 - e^{(-6.55 \cdot V_f)}\right) \tag{7}$$

This angle serves to identify the second point of the diagram (point k), which is the intersection of the softening function of plain concrete (here considered as an exponential function: $\sigma = f_t \cdot \exp(-\frac{f_t \cdot w}{G_F})$) with a line passing through the origin with a direction defined by ϕ (see Figure 5).

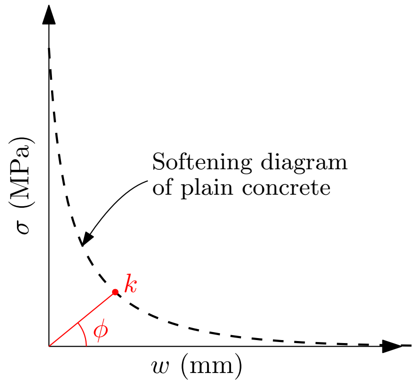

Figure 5: Identification of k point of the trilinear diagram by means of the angle ϕ.

By using the three main parameters mentioned before and the ultimate tensile strength of the fibres (σ_u), the maximum remaining strength (σ_r) can be obtained with (8).

$$\sigma_r = (1 - \%Pulled - out) \cdot V_f \cdot \theta \cdot \sigma_u \tag{8}$$

Considering the scheme of the trilinear diagram shown in Figure 1, the first two points can be identified as follows: point t is identified by f_t, which can be experimentally obtained, while point k depends on the volume fraction of fibres (V_f) by means of the ϕ angle defined with (7) and the softening function of plain concrete. Table 4 shows the intermediate values that result of this calculation.

As regards the remaining two points, r and f, the value of σ_r can be obtained with (8). Table 5 shows the results of this calculation for each size, and σ_f is, obviously, equal to 0, but w_r and w_f must be estimated; they depend on the fibre length, but there are no specific expressions to obtain them. In this case,

Table 4: Intermediate values for obtaining point k of the trilinear diagram.

	f_t (MPa)	G_F (N/mm)	ϕ	w_k (mm)	σ_k (MPa)
Small/Medium/Large	3.2	0.13	1.448	0.07143	0.57715

w_r is estimated as equal to 1.65 mm, since this was the value adopted in (Suárez, Gálvez, Enfedaque, & Alberti 2019) for simulating fracture in specimens made with 48 mm long fibres of the same kind as those used here. As regards w_f, this value is related to the maximum crack opening before completely losing the bonding between the fibres and the matrix; therefore, it is assumed to be proportional to the fibre length. Thus, since in (Alberti, Enfedaque, Gálvez, & Reyes 2017) specimens made with 60 mm long fibres were modelled using $w_f = 7.5$ mm, here, a value of $w_f = \frac{48}{60} \cdot 7.5 = 6.0$ mm is adopted. Figure 6 shows the resulting trilinear softening diagrams for all three sizes.

5 RESULTS AND DISCUSSION

Fracture of the three specimen sizes analysed in (Alberti, Enfedaque, & Gálvez 2015) was carried out using the finite element method, and a displacement control was used to drive the fracture evolution with good convergence. The simulations were computed using ABAQUS (Smith 2009), and the fracture was reproduced by means of a UMAT subroutine that implemented the previously described material behaviour.

Figure 7 shows the three meshes used in this work with the same scale. In all three meshes, the region connecting the notch tip with the load application point was refined in order to better capture the fracture process, while the rest of the specimen was meshed with larger elements, which helped to notably reduce the time of computation. The models were formed by a number of nodes smaller than 800 and a number of triangular finite elements smaller than 1500, thus keeping the model size small enough to have models that perform efficiently. These simulations were run on a computer with an Intel Xeon E5-1620 processor with 4 cores at 3.5 GHz, although only one was used since the user subroutine that reproduces the material behaviour does not allow parallel computing; all the simulations took around 150 min to run. In the case of the large size model (L), the side of minimum element size was around 7 mm, in the case of the medium size model (M), 3.5 mm, and in the case of the small size model (S), 2 mm. The refinement of these meshes was designed based on previous works (see (Suárez, Gálvez, Enfedaque, & Alberti 2019)), in which the mesh dependence was already analysed.

Figure 8 shows the load–load displacement and load–CMOD diagrams for all three sizes and compares them with the experimental results. Each specimen size is identified by a different colour: red for large size, blue for medium size, and green for small size. The shades behind the diagrams correspond to the experimental envelopes, with the same colour code used in the diagrams; therefore, the red shade corresponds to the experimental envelope of the large specimens, the blue shade to the experimental envelope of medium specimens, and the green shade to the experimental envelope of small specimens. Apart from the overestimation of the initial peak, which is a known issue when this type of numerical modelling is used, especially in large-sized specimens (Elices, Guinea, Gómez, & Planas 2002), the models reproduce the experimental results reasonably well. This agreement is particularly good, in the case of the medium size, and presents some differences in the last part of the load–load displacement diagrams, in the cases of large and small sizes, in which the numerical model tends to underestimate the specimen's remaining strength.

It is also worth noting that in the case of the experimental results, the maximum remanent load occurs at a larger load displacement if compared with the medium and large sizes, while in the case of the numerical results, this maximum load after the first peak occurs approximately at the same load displacement and, in all cases, following a very linear trend. These trends are depicted by dashed lines on the load–load displacement diagrams of Figure 8.

These results show that expressions (7) and (8), defined in the past by analysing the fracture behaviour of different PFRC mixes, well describe the general behaviour of this material and take into account the main parameters: the volume of fibres in the mix (V_f), the orientation of fibres with respect to the fracture surface (θ), and the quality of bonding between the fibres and concrete, expressed by the fraction of fibres that are pulled out at the fracture surface ($\%Pulled - out$). Nevertheless, the parameters used to define the trilinear softening diagrams, abscissa values of points k and f, are only estimated based on previous experiences with this type of model, but there are no expressions proposed for them yet. In the following section, the influence of these two values, w_r and w_f, is studied to understand how they modify the diagrams, which can help to propose expressions to quantify them.

Table 5: Intermediate values for obtaining σ_r for all three considered sizes.

	θ	$\%Pulled-Out$	V_f	σ_u (MPa)	σ_r (MPa)
Small	0.63	0.54	0.011	376	1.20
Medium	0.62	0.54	0.011	376	1.18
Large	0.72	0.54	0.011	376	1.37

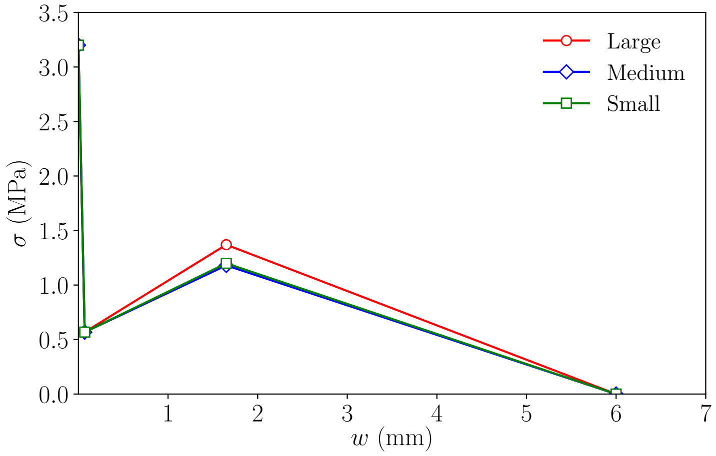

Figure 6: Initial trilinear softening diagrams.

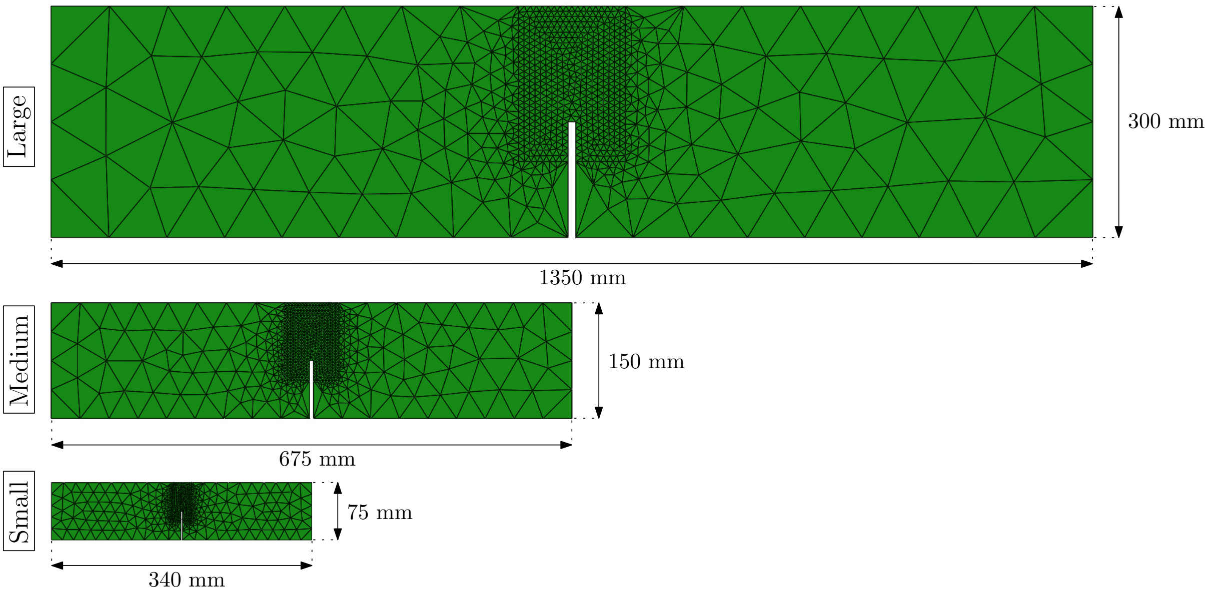

Figure 7: FEM meshes used in the simulations for each specimen size.

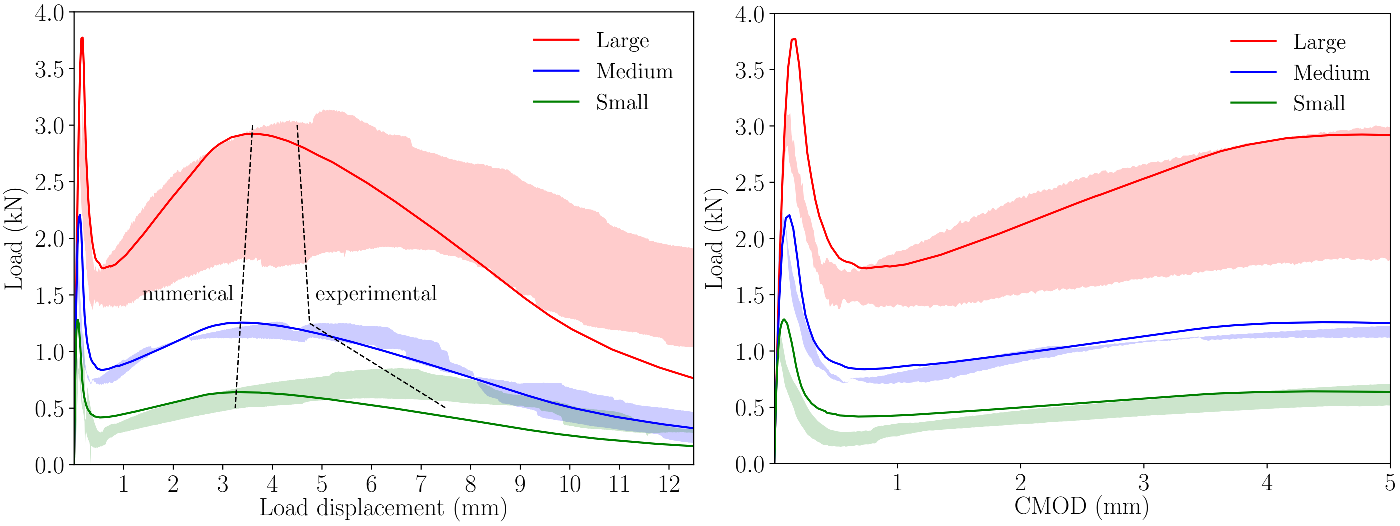

Figure 8: Numerical results compared with the experimental envelopes; each specimen size is identified by a different colour. Experimental envelopes correspond to three specimens tested.

6 CONCLUSIONS

In this work, the numerical modelling of the size effect by means of a cohesive model fed with a trilinear softening function was studied using a predictive method. A three-point bending test on specimens of three sizes was numerically reproduced and compared with experimental data from previous works. The trilinear diagrams for each size were defined by expressions obtained in previous experimental campaigns, resulting in good agreement with the lab observations.

From the work presented above, the following conclusions can be drawn:

1. The complete fracture behaviour of PFRC specimens can be numerically simulated using a predictive trilinear cohesive crack model, which can be defined a priori by means of empirical expressions obtained with lab tests different from those simulated. This diagram is defined by four points, with coordinates that depend on PFRC mechanical characteristics, i.e., the tensile strength of the matrix, the proportion of fibres, and the orientation factor. Abscissa values w_r and w_f (see Figure 3) are fixed based on experimental results obtained in previous literature. It is still an unsolved challenge to obtain expressions to estimate w_r and w_f using the mechanical characteristics of the PFRC.

2. The softening diagrams are not equal for all specimen sizes and should be adjusted for each of them. This is mainly due to a different orientation factor that varies with the size of the specimen.

3. The maximum remanent loads obtained for each size present a linear trend on the load–displacement diagram, which does not agree completely with the experimental observations, although the load–displacement and load–CMOD curves properly agree with the experimental envelopes for the three studied sizes.

ACKNOWLEDGEMENTS

The authors gratefully acknowledge the financial support provided for this research by the Ministry of Science and Innovation of Spain through the Research Fund Project PID2019-108978RB-C31.

REFERENCES

Alberti, M., A. Enfedaque, & J. Gálvez (2015). Comparison between polyolefin fibre reinforced vibrated conventional concrete and self-compacting concrete. *Construction and Building Materials 85*, 182 – 194.

Alberti, M., A. Enfedaque, & J. Gálvez (2017). Fibre reinforced concrete with a combination of polyolefin and steel-hooked fibres. *Composite Structures 171*, 317–325.

Alberti, M., A. Enfedaque, J. Gálvez, & V. Agrawal (2016). Fibre distribution and orientation of macro-synthetic polyolefin fibre reinforced concrete elements. *Construction and Building Materials 122*, 505–517.

Alberti, M., A. Enfedaque, J. Gálvez, & A. Cortez (2020). Optimisation of fibre reinforcement with a combination strategy and through the use of self-compacting concrete. *Construction and Building Materials 235*, 117289.

Alberti, M., A. Enfedaque, J. Gálvez, & E. Reyes (2017). Numerical modelling of the fracture of polyolefin fibre reinforced concrete by using a cohesive fracture approach. *Composites Part B: Engineering 111*, 200 – 210.

Alberti, M. G., J. C. Gálvez, A. Enfedaque, A. Carmona, C. Valverde, & G. Pardo (2018). Use of steel and polyolefin fibres in the la canda tunnels: Applying mives for assessing sustainability evaluation. *Sustainability 10*(12), 4765.

Banthia, N. & R. Gupta (2006). Influence of polypropylene fiber geometry on plastic shrinkage cracking in concrete. *Cement and Concrete Research 36*(7), 1263–1267.

Barenblatt, G. I. (1962). The mathematical theory of equilibrium cracks in brittle fracture. In *Advances in applied mechanics*, Volume 7, pp. 55–129. Elsevier.

Bažant, Z. P. (1984). Size effect in blunt fracture: concrete, rock, metal. *Journal of engineering mechanics 110*(4), 518–535.

Bažant, Z. P. & J. Planas (1997). *Fracture and size effect in concrete and other quasibrittle materials*. CRC press.

Bažant, Z. P. & Q. Yu (2009). Universal size effect law and effect of crack depth on quasi-brittle structure strength. *Journal of engineering mechanics 135*(2), 78–84.

Brandt, A. M. (2008). Fibre reinforced cement-based (frc) composites after over 40 years of development in building and civil engineering. *Composite Structures 86*(1), 3–9. Fourteenth International Conference on Composite Structures.

di Prisco, M., R. Felicetti, M. Lamperti, & G. Menotti (2004). On size effect in tension of sfrc thin plates. *Fracture mechanics of concrete structures 2*, 1075–1082.

Di Prisco, M., M. Lamperti, S. Lapolla, & R. S. Khurana (2008). Hpfrcc thin plates for precast roofing. In *Proceedings of the 2nd international symposium on HPC, Kassel*.

Dugdale, D. S. (1960). Yielding of steel sheets containing slits. *J Mech Phys Solids 8*(2), 100–104.

Elices, M., G. Guinea, J. Gómez, & J. Planas (2002). The cohesive zone model: advantages, limitations and challenges. *Engineering fracture mechanics 69*(2), 137–163.

Enfedaque, A., M. Alberti, J. Gálvez, & J. Domingo (2017). Numerical simulation of the fracture behaviour of glass fibre reinforced cement. *Construction and Building Materials 136*, 108 – 117.

Enfedaque, A., M. G. Alberti, & J. C. Gálvez (2019). Influence of fiber distribution and orientation in the fracture behavior of polyolefin fiber-reinforced concrete. *Materials 12*(2), 220.

Enfedaque, A., M. G. Alberti, J. C. Gálvez, M. Rivera, & J. Simón-Talero (2018). Can polyolefin fibre reinforced concrete improve the sustainability of a flyover bridge? *Sustainability 10*(12), 4583.

European Committee for Standardization (2007). Test method for metallic fibre concrete. measuring the flexural tensile strength (limit of proportionality (lop), residual).

Gálvez, J., J. Planas, J. Sancho, E. Reyes, D. Cendón, & M. Casati (2013). An embedded cohesive crack model for finite element analysis of quasi-brittle materials. *Eng Fract Mech 109*, 369–386.

Hillerborg, A., M. Modéer, & P.-E. Petersson (1976). Analysis of crack formation and crack growth in concrete by means of fracture mechanics and finite elements. *Cem Concr Res 6*(6), 773 – 781.

Jirásek, M., S. Rolshoven, & P. Grassl (2004). Size effect on fracture energy induced by non-locality. *International Jour-*

nal for Numerical and Analytical Methods in Geomechanics 28(7-8), 653–670.

Picazo, Á., M. G. Alberti, J. C. Gálvez, A. Enfedaque, & A. C. Vega (2019). The size effect on flexural fracture of polyolefin fibre-reinforced concrete. *Applied Sciences 9*(9), 1762.

Picazo, A., J. Gálvez, M. Alberti, & A. Enfedaque (2018). Assessment of the shear behaviour of polyolefin fibre reinforced concrete and verification by means of digital image correlation. *Construction and Building Materials 181*, 565–578.

Planas, J., G. Guinea, & M. Elices (1999). Size effect and inverse analysis in concrete fracture. *International Journal of Fracture 95*(1-4), 367.

Reyes, E., J. Gálvez, M. Casati, D. Cendón, J. Sancho, & J. Planas (2009). An embedded cohesive crack model for finite element analysis of brickwork masonry fracture. *Engineering Fracture Mechanics 76*(12), 1930 – 1944.

Sancho, J., J. Planas, D. Cendón, E. Reyes, & J. Gálvez (2007). An embedded crack model for finite element analysis of concrete fracture. *Engineering Fracture Mechanics 74*(1), 75 – 86. Fracture of Concrete Materials and Structures.

Shah, S. P. & B. V. Rangan (1971). Fiber reinforced concrete properties. In *Journal Proceedings*, Volume 68, pp. 126–137.

Smith, M. (2009). *ABAQUS/Standard User's Manual, Version 6.9*. United States: Dassault Systèmes Simulia Corp.

Suárez, F., J. Gálvez, A. Enfedaque, & M. Alberti (2019). Modelling fracture on polyolefin fibre reinforced concrete specimens subjected to mixed-mode loading. *Engineering Fracture Mechanics 211*, 244 – 253.

Ward, R. & V. Li (1991). Dependence of flexural behaviour of fibre reinforced mortar on material fracture resistance and beam size. *Construction and Building Materials 5*(3), 151–161.

Yoo, D.-Y., N. Banthia, J.-M. Yang, & Y.-S. Yoon (2016). Size effect in normal- and high-strength amorphous metallic and steel fiber reinforced concrete beams. *Construction and Building Materials 121*, 676 – 685.

Zollo, R. F. (1997). Fiber-reinforced concrete: an overview after 30 years of development. *Cement and Concrete Composites 19*(2), 107–122.